Magnetointerferometry of multiterminal Josephson junctions

Régis Mélin [1,*] Clemens B. Winkelmann,[2] and Romain Danneau [3]
[1]Institut NEEL, Université Grenoble-Alpes, CNRS, Grenoble INP, Grenoble, France
[2]IRIG-Pheliqs, Université Grenoble-Alpes, CEA, Grenoble INP, Grenoble, France
[3]Institute for Quantum Materials and Technologies, Karlsruhe Institute of Technology, Karlsruhe D-76021, Germany

(Received 21 November 2023; revised 30 January 2024; accepted 20 February 2024; published 6 March 2024)

We report a theoretical study of multiterminal Josephson junctions under the influence of a magnetic field B. We consider a ballistic rectangular two-dimensional metal N_0 connected by the edges to the left, right, top, and bottom superconductors S_L, S_R, S_T, and S_B, respectively. We numerically calculate in the large-gap approximation the critical current I_c versus B between the left and right S_L and S_R for various aspect ratios, with the top and bottom S_T and S_B playing the role of superconducting mirrors. We find the critical current I_c to be enhanced by orders of magnitude, especially at long distance, due to the phase rigidity provided by the mirrors. We obtain magnetic oscillations resembling those of a superconducting quantum interference device. With symmetric couplings, the self-consistent superconducting phase variables of the top and bottom mirrors take the values 0 or π, as for emerging Ising degrees of freedom. We propose a simple effective Josephson junction circuit model that is compatible with these microscopic numerical calculations. From the $I_c(B)$ patterns we infer where the supercurrent flows in various device geometries. In particular in the elongated geometry, we show that the supercurrent flows between all pairs of contacts, which allows exploring the full phase space of the relevant phase differences.

DOI: 10.1103/PhysRevB.109.125406

I. INTRODUCTION

Superconducting multiterminal systems have recently attracted considerable attention. While early theoretical works already predicted unusual behavior of these more complex Josephson junctions [1–4], later ones demonstrated that these systems may host several exotic phenomena such as correlations among Cooper pairs known as the quartets [5–17] as well as Weyl point singularities and nontrivial topology in the Andreev bound state spectrum [18–32], and the energy level repulsion in Andreev molecules [33–36]. Following these theoretical efforts, recent experiments have reported the detection of Cooper quartets [37–40], the observation of Floquet-Andreev states [41], the studies of Andreev molecules [42–45], the multiterminal superconducting diode effect [46,47], in addition to other results using numerous different types of superconducting weak links [48–55].

The common ground of these models and experiments is related to the fact that the weak links are connected by, at least, three superconducting contacts. Indeed, in comparison to its two-lead counterparts, the supercurrent flow in multiterminal Josephson junctions may appear nontrivial. Seminal works showed that the supercurrent distribution could be probed by analyzing the interference pattern induced by the application of a magnetic flux across two-terminal Josephson junctions [56–60]. Therefore, this interferometric pattern strongly depends on the device geometry and where the supercurrent flows [61–73]. As shown by Dynes and Fulton [57], in two-terminal Josephson junctions, the magnetic field dependence of the critical current is related to the supercurrent density distribution across the device by an inverse Fourier transform as long as the supercurrent density is constant along the current flow. However, alternative models are needed in the case of nonhomogeneous supercurrent density [70] or nonregular shapes [71,73].

To our knowledge, no theories exploring the current flow and the corresponding magnetointerferometric pattern in multiterminal Josephson junctions are available so far. Here, we present a microscopic model allowing us to calculate the magnetic field dependence of the critical current in various configurations (see Fig. 1). Our calculations are based on a large-gap Hamiltonian in which the supercurrent is triggered by the *tracer* of the phase of the vector potential, i.e., we calculate the critical current pattern as a function of the magnetic field. While we recover the standard two-terminal interferometric patterns, we show that the additional lead drastically modifies the magnetic field dependence of the critical current. With four terminals, our calculations reveal that the supercurrent visits all of the superconducting leads, which could result from a kind of ergodicity. This notion of ergodicity was lately pointed out via the studies of the critical current contours (CCCs) in four-terminal Josephson junctions, as a function of two different biasing currents [11,49]. Consistency was demonstrated [49] between the experiments on the CCCs and random matrix theory, where the scattering matrix bridges all of the superconducting leads. Considering disorder in the short-junction limit, quantum chaos leads to ergodicity in the sense of Andreev bound states (ABS) coupling all of the superconducting leads. The supercurrent significantly visits

*regis.melin@neel.cnrs.fr

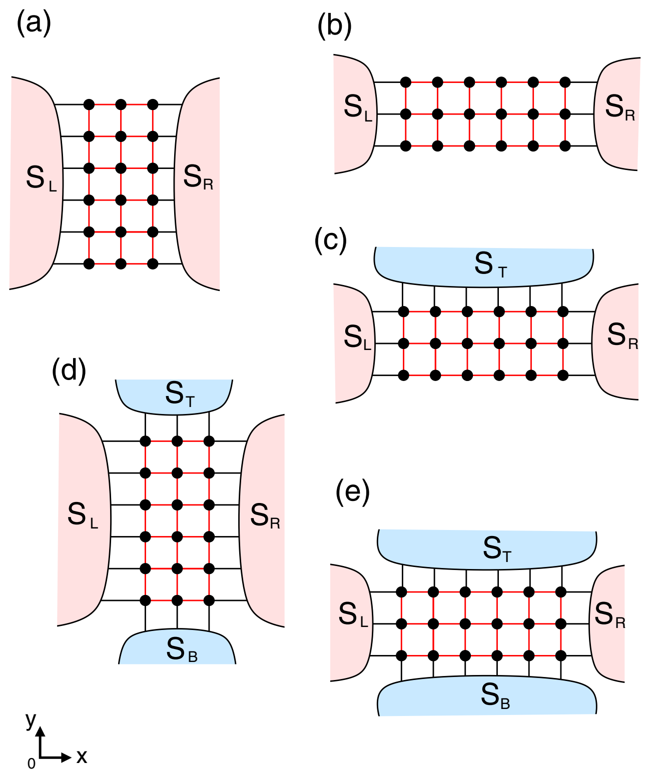

FIG. 1. Schematics of the considered two- and multiterminal Josephson geometries. The superconductors S_T and S_B on top and bottom are in open circuit, that is, they are superconducting mirrors, and we calculate the current flowing horizontally from S_L to S_R. A four-terminal device with $N = 3$ and $M = 6$ is shown in panel (a), i.e., a device with $M/N \gtrsim 1$ elongated in the vertical y-axis direction. A two-terminal device elongated in the horizontal x-axis direction is shown on panel (b) with $N = 6$ and $M = 3$, i.e., with $M/N \lesssim 1$. Panels (c), (d), and (e) feature three- or four-terminal devices containing a single or two superconducting mirrors, and elongated along the x- or y-axis direction.

all of those n superconducting terminals, thus being sensitive to $n-1$ independent phase differences, a number that is, however, reduced by the additional constraints of current conservation imposed by the external sources. In the other limit of large-scale devices, another recent work [74] pointed out the relevance of long-range effects in multiterminal configurations, as the result of the phase rigidity.

Here, we also find long-range propagation of the supercurrent in three- or four-terminal geometry having one or two superconducting mirrors respectively, due to the phase rigidity in the leads under zero-current bias condition. In the four-terminal geometries, the leads S_L, S_R, S_T, and S_B are connected to the left, right, top, and bottom sides of the rectangular normal-metallic conductor N_0, and S_T, S_B are laterally connected on top and bottom, being superconducting mirrors in open circuit, as shown Figs. 1(c) and 1(d). For the elongated geometry along the horizontal x-axis direction [see Fig. 1(c)], the four-terminal magnetic oscillations of the critical current resemble the pattern of a superconducting quantum interference device (SQUID) because of the interfering supercurrent paths propagating in S_T and S_B over long distance. The critical current in the horizontal direction is controlled by the phases φ_T and φ_B of the top and bottom superconductors S_T and S_B. Symmetry in the hopping amplitudes connecting N_0 to the four superconductors leads to the discrete values $\varphi_T, \varphi_B = 0$ or π, as for emerging Ising degrees of freedom.

Finally, a simple phenomenological Josephson junction circuit model is proposed for devices elongated in the horizontal direction. In this model, both of the superconducting phase variables φ_T and φ_B enter the critical current via their difference $\varphi_T - \varphi_B$, which originates from the large Josephson energy coming from the extended interfaces parallel to the horizontal direction.

The paper is organized as follows. The model and Hamiltonians are presented in Sec. II. The numerical results are presented and discussed in Sec. III. Section IV presents a phenomenological Josephson junction circuit model. Concluding remarks are provided in Sec. V.

II. MODEL AND HAMILTONIANS

In this section, we define the Hamiltonian of the devices shown in Fig. 1. The Hamiltonians of each part of the circuit are provided in Sec. II A. The large-gap Hamiltonian of the entire structure is presented in Sec. II B, and the boundary conditions in the presence of a magnetic field are next discussed in Sec. II C. The algorithm is presented in Sec. II D.

A. General Hamiltonians

In this subsection, we introduce the Hamiltonians of the superconductor, the central normal-metal conductor, and the coupling between them.

The superconductors are described by the BCS Hamiltonian

$$\hat{\mathscr{H}}_{\mathrm{BCS}} = -W \sum_{\langle i,j\rangle} \sum_{\sigma_z=\uparrow,\downarrow} (c^+_{i,\sigma_z} c_{j,\sigma_z} + c^+_{j,\sigma_z} c_{i,\sigma_z}) \tag{1}$$

$$- \Delta \sum_k (\exp{(i\varphi_k)} c^+_{k,\uparrow} c^+_{k,\downarrow} + \exp{(-i\varphi_k)} c_{k,\downarrow} c_{k,\uparrow}), \tag{2}$$

where the summation in the first term is over all pairs of neighboring tight-binding sites $\langle i, j\rangle$ and over the projection σ_z on the spin quantization axis, that is the z axis. The first term given by Eq. (1) corresponds to the kinetic energy, i.e., to spin-σ_z electrons hopping between neighboring tight-binding sites on a square lattice. The second term given by Eq. (2) is the mean field BCS pairing term, with superconducting phase variable φ_k at the tight-binding site k. The superconducting phase variables φ_k take different values between different superconducting leads and the φ_k's are assumed to be uniform within each of those since we handle weak currents throughout the paper. In order to reduce the computational expanses, we carry out the calculations in a regime where the superconducting gap is the largest energy scale, leading to a *large-gap Hamiltonian* for the entire device connected to the superconducting leads. This approach will be justified from qualitative agreement with the known Fraunhofer pattern as in a two-terminal configuration [i.e., with vanishingly small coupling to the top and bottom S_T and S_B respectively; see Figs. 1(a) and 1(b)].

The central ballistic normal-metallic conductor N_0 is described by the square-lattice tight-binding Hamiltonian on a rectangle of dimensions $Na_0\times Ma_0$ in the horizontal x- and vertical y-axis directions respectively, where a_0 is the lattice spacing:

$$\hat{\mathcal{H}}_{\Sigma^{(0)}} = -\Sigma^{(0)}\sum_{\langle i,j\rangle}\sum_{\sigma_z=\uparrow,\downarrow}(c^+_{i,\sigma_z}c_{j,\sigma_z}+c^+_{j,\sigma_z}c_{i,\sigma_z}), \quad (3)$$

with hopping amplitude $\Sigma^{(0)}$. Equation (3) is intended to qualitatively capture a two-dimensional conductor at high charge carrier density, and thus presenting a well-defined extended Fermi surface. We assume that a finite gate voltage is applied to the square-lattice tight-binding Hamiltonian of Eq. (3) in such a way as to avoid the square-lattice midband singularities:

$$\hat{\mathcal{H}}_g = -W_g\sum_{k,\sigma_z}c^+_{k,\sigma_z}c_{k,\sigma_z}. \quad (4)$$

The contacts between the normal and superconducting leads are captured by the following tight-binding Hamiltonian with hopping amplitude $\Sigma^{(1)}$:

$$\hat{\mathcal{H}}_{\Sigma^{(1)}} = -\Sigma^{(1)}\sum_{\langle i',j'\rangle}\sum_{\sigma_z=\uparrow,\downarrow}(c^+_{i',\sigma_z}c_{j',\sigma_z}+c^+_{j',\sigma_z}c_{i',\sigma_z}), \quad (5)$$

where $\sum_{\langle i',j'\rangle}$ runs over all tight-binding sites on both sides of the contact.

The magnetic field is included by adding a phase to the hopping amplitudes between the tight-binding sites a and b:

$$\Sigma_{a\to b}\to\Sigma_{a\to b}\exp\left(\frac{ie}{\hbar}\int_a^b\mathbf{A}\cdot d\mathbf{s}\right), \quad (6)$$

where $\mathbf{A}$ is the vector potential. In addition, the absence of screening currents on the superconducting sides of the normal metal-superconductor boundaries will be taken into account according to the forthcoming Sec. II C.

B. Large-gap Hamiltonian at zero magnetic field

In this subsection, we consider that the superconducting gaps are the largest energy scales. This yields a large-gap Hamiltonian for the entire device, which will afterwards be treated via exact diagonalizations. The DC-Josephson currents are obtained from numerically differentiating the ground state energy with respect to the superconducting phase variable of the corresponding terminal. Making the approximation of a large superconducting gap was developed in recent years; see for instance Refs. [15,25,75,76]. Reaching numerical efficiency for large-scale devices is the main motivation for this large-gap limit.

Large-gap Hamiltonian from wave-functions. Now, we present a wave-function calculation which yields the large-gap Hamiltonian. Using generic compact matrix notations, the starting-point Nambu Hamiltonian is expressed as the sum of three terms:

(i) *The infinite Nambu matrix of the superconducting tight-binding Hamiltonian* $\hat{\mathcal{H}}_{S,S}$ is deduced from the BCS Hamiltonian $\hat{\mathcal{H}}_{\rm BCS}$ in Eqs. (1) and (2). Those superconducting leads are generically denoted as $S_1,\dots,S_n$ and $\hat{\mathcal{H}}_{S,S}$ is a matrix gathering all of the $\hat{\mathcal{H}}_{S_p,S_p}$, with $p=1,\dots,n$.

In order to illustrate the discussion, we consider for simplicity that the lead S_p contains two tight-binding sites labeled by "1" and "2", which yields the following 4×4 Nambu Hamiltonian $\hat{\mathcal{H}}_{S_p,S_p}$:

$$\hat{\mathcal{H}}_{S_p,S_p}=\begin{pmatrix}0 & \Delta_pe^{i\varphi_p} & -W_{1,2} & 0\\ \Delta_pe^{-i\varphi_p} & 0 & 0 & W_{1,2}\\ -W_{2,1} & 0 & 0 & \Delta_pe^{i\varphi_p}\\ 0 & W_{2,1} & \Delta_pe^{-i\varphi_p} & 0\end{pmatrix}. \quad (7)$$

With a three-site tight-binding cluster, we obtain the following 6×6 Nambu Hamiltonian:

$$\hat{\mathcal{H}}_{S_p,S_p} = \begin{pmatrix}0 & \Delta_pe^{i\varphi_p} & -W_{1,2} & 0 & -W_{1,3} & 0\\ \Delta_pe^{-i\varphi_p} & 0 & 0 & W_{1,2} & 0 & W_{1,3}\\ -W_{2,1} & 0 & 0 & \Delta_pe^{i\varphi_p} & -W_{2,3} & 0\\ 0 & W_{2,1} & \Delta_pe^{-i\varphi_p} & 0 & 0 & W_{2,3}\\ -W_{3,1} & 0 & -W_{3,2} & 0 & 0 & \Delta_pe^{i\varphi_p}\\ 0 & W_{3,1} & 0 & W_{3,2} & \Delta_pe^{-i\varphi_p} & 0\end{pmatrix}, \quad (8)$$

where the three tight-binding sites are labeled by 1, 2, and 3. The matrices in Eqs. (7) and (8) can be extrapolated to an infinite number of tight-binding sites, also taking the connectivity of the underlying lattice into account. Finally, all of the $\hat{\mathcal{H}}_{S_p,S_p}$ are concatenated into the global $\hat{\mathcal{H}}_{S,S}$ matrix.

(ii) *The finite Nambu matrix rectangular normal-metal tight-binding lattice Hamiltonian* $\hat{\mathcal{H}}_{N_0,N_0}$ is deduced from $\hat{\mathcal{H}}_{\Sigma^{(0)}}$ in Eq. (3) and $\hat{\mathcal{H}}_g$ in Eq. (4). The Nambu Hamiltonian $\hat{\mathcal{H}}_{N_0,N_0}$ takes the following form for the two tight-binding sites labeled by 1 and 2:

$$\hat{\mathcal{H}}^{2\times2}_{N_0,N_0}=\begin{pmatrix}W_g & 0 & -\Sigma^{(0)}_{1,2} & 0\\ 0 & -W_g & 0 & \Sigma^{(0)}_{1,2}\\ -\Sigma^{(0)}_{2,1} & 0 & W_g & 0\\ 0 & \Sigma^{(0)}_{2,1} & 0 & -W_g\end{pmatrix}. \quad (9)$$

We obtain the following with the three tight-binding sites labeled by 1, 2, and 3:

$$\hat{\mathcal{H}}^{3\times3}_{N_0,N_0}=\begin{pmatrix}W_g & 0 & -\Sigma^{(0)}_{1,2} & 0 & -\Sigma^{(0)}_{1,3} & 0\\ 0 & -W_g & 0 & \Sigma^{(0)}_{1,2} & 0 & \Sigma^{(0)}_{1,3}\\ -\Sigma^{(0)}_{2,1} & 0 & W_g & 0 & -\Sigma^{(0)}_{2,3} & 0\\ 0 & \Sigma^{(0)}_{2,1} & 0 & -W_g & 0 & \Sigma^{(0)}_{2,3}\\ -\Sigma^{(0)}_{3,1} & 0 & -\Sigma^{(0)}_{3,2} & 0 & W_g & 0\\ 0 & \Sigma^{(0)}_{3,1} & 0 & \Sigma^{(0)}_{3,2} & 0 & -W_g\end{pmatrix}, \quad (10)$$

and Eqs. (9) and (10) are easily generalized to an arbitrary number of entries.

(iii) *The finite Nambu matrix of the couplings* $\hat{\mathcal{H}}_{N_0,S}$ *and* $\hat{\mathcal{H}}_{S,N_0}$ *between the superconductors* S_p *and the normal region* N_0 is deduced from $\hat{\mathcal{H}}_{\Sigma^{(1)}}$ in Eq. (5). The Nambu Hamiltonian

$\hat{\mathscr{H}}_{N_0,S_p}$ takes the following form with interfaces made with the two tight-binding sites labeled by 1 and 2:

$$\hat{\mathscr{H}}^{2\times 2}_{N_0,S_p} = \begin{pmatrix} 0 & 0 & -\Sigma^{(1)}_{1,2} & 0 \\ 0 & 0 & 0 & \Sigma^{(1)}_{1,2} \\ -\Sigma^{(1)}_{2,1} & 0 & 0 & 0 \\ 0 & \Sigma^{(1)}_{2,1} & 0 & 0 \end{pmatrix}, \tag{11}$$

and we obtain the following for interfaces made with the three tight-binding sites labeled by 1, 2, and 3:

$$\hat{\mathscr{H}}^{3\times 3}_{N_0,S_p} = \begin{pmatrix} 0 & 0 & -\Sigma^{(1)}_{1,2} & 0 & -\Sigma^{(1)}_{1,3} & 0 \\ 0 & 0 & 0 & \Sigma^{(1)}_{1,2} & 0 & \Sigma^{(1)}_{1,3} \\ -\Sigma^{(1)}_{2,1} & 0 & 0 & 0 & -\Sigma^{(1)}_{2,3} & 0 \\ 0 & \Sigma^{(1)}_{2,1} & 0 & 0 & 0 & \Sigma^{(1)}_{2,3} \\ -\Sigma^{(1)}_{3,1} & 0 & -\Sigma^{(1)}_{3,2} & 0 & 0 & 0 \\ 0 & \Sigma^{(1)}_{3,1} & 0 & \Sigma^{(1)}_{3,2} & 0 & 0 \end{pmatrix}, \tag{12}$$

and the matrices appearing in Eqs. (11) and (12) can be extended to an arbitrary number of entries.

The components of the Bogoliubov–de Gennes wavefunctions are denoted as ψ_{N_0} and ψ_S for the normal conductor N_0 and the n superconducting leads S_p respectively, with $p = 1, \ldots, n$. Each of the ψ_{N_0} and ψ_S is defined on the normal-metallic tight-binding graph N_0 and in all tight-binding sites of each superconductor S_p.

The overall infinite Nambu Hamiltonian $\hat{\mathscr{H}}$ takes the following matrix form:

$$\hat{\mathscr{H}} = \begin{pmatrix} \hat{\mathscr{H}}_{N_0,N_0} & \hat{\mathscr{H}}_{N_0,S} \\ \hat{\mathscr{H}}_{S,N_0} & \hat{\mathscr{H}}_{S,S} \end{pmatrix}. \tag{13}$$

The Bogoliubov–de Gennes eigenvalue equation is defined as

$$\hat{\mathscr{H}} \begin{pmatrix} \psi_{N_0} \\ \psi_S \end{pmatrix} = \omega \begin{pmatrix} \psi_{N_0} \\ \psi_S \end{pmatrix}, \tag{14}$$

where ω is the energy, and Eq. (14) leads to the following set of equations:

$$\hat{\mathscr{H}}_{N_0,N_0}\psi_{N_0} + \hat{\mathscr{H}}_{N_0,S}\psi_S = \omega\psi_{N_0}, \tag{15}$$

$$\hat{\mathscr{H}}_{S,N_0}\psi_{N_0} + \hat{\mathscr{H}}_{S,S}\psi_S = \omega\psi_S, \tag{16}$$

where Eqs. (15) and (16) contain a finite and an infinite number of equations respectively. Equation (16) is written as follows:

$$\psi_S = (\omega - \hat{\mathscr{H}}_{S,S})^{-1}\hat{\mathscr{H}}_{S,N_0}\psi_{N_0}. \tag{17}$$

Equation (17) is now specialized to the Nambu components of the superconducting Green's functions defined on the superconducting side of the coupling Nambu Hamiltonians $\hat{\mathscr{H}}_{N_0,S}$ and $\hat{\mathscr{H}}_{S,N_0}$. Then, inserting Eq. (17) into Eq. (15) leads to an eigenvalue problem for a finite number of linear equations:

$$\hat{\mathscr{H}}_{N_0,N_0}\psi_{N_0} + \hat{\mathscr{H}}_{N_0,S}(\omega - \hat{\mathscr{H}}_{S,S})^{-1}\hat{\mathscr{H}}_{S,N_0}\psi_{N_0} = \omega\psi_{N_0}. \tag{18}$$

This defines the effective self-energy $\hat{\Sigma}_{\text{eff}}(\omega)$ as

$$\hat{\Sigma}_{\text{eff}}(\omega)\psi_{N_0} = \omega\psi_{N_0}, \tag{19}$$

with

$$\hat{\Sigma}_{\text{eff}}(\omega) = \hat{\mathscr{H}}_{N_0,N_0} + \hat{\mathscr{H}}_{N_0,S}(\omega - \hat{\mathscr{H}}_{S,S})^{-1}\hat{\mathscr{H}}_{S,N_0} \tag{20}$$

$$= \hat{\mathscr{H}}_{N_0,N_0} + \hat{\Sigma}^{(1)}_{N_0,S}\hat{g}_{S,S}(\omega)\hat{\Sigma}^{(1)}_{S,N_0}, \tag{21}$$

where

$$\hat{g}_{S,S}(\omega) = (\omega - \hat{\mathscr{H}}_{S,S})^{-1} \tag{22}$$

is the resolvent (i.e., the Green's function) of the infinite superconducting leads and $\hat{\Sigma}^{(1)}_{N_0,S}$ and $\hat{\Sigma}^{(1)}_{S,N_0}$ are the Nambu hopping amplitudes in $\hat{\mathscr{H}}_{N_0,S}$ and $\hat{\mathscr{H}}_{S,N_0}$ respectively; see also Eq. (5).

Up to this point the superconducting gap was finite, but now we take the limit of a large gap where $\hat{g}_{S,S}(\omega)$ becomes independent of the energy ω, i.e., $\hat{g}_{S,S}(\omega) \equiv \hat{g}_{S,S}$ [see the forthcoming Eqs. (27) and (28) for the expression of the superconducting Green's functions.] The effective self-energy $\hat{\Sigma}_{\text{eff}}(\omega)$ in Eqs. (20) and (21) takes the form of the following energy-independent effective Hamiltonian:

$$\hat{\Sigma}_{\text{eff}}(\omega) \equiv \hat{\mathscr{H}}_{\text{eff}} = \hat{\mathscr{H}}_{N_0,N_0} + \hat{\Sigma}^{(1)}_{N_0,S}\hat{g}_{S,S}\hat{\Sigma}^{(1)}_{S,N_0}. \tag{23}$$

Large-gap Hamiltonian from Green's functions. The large-gap Hamiltonian given by Eq. (23) can also be obtained from the Dyson equations; see Ref. [15]. Namely, the fully dressed Green's function $\hat{G}_{N_0,N_0}(\omega)$ at the energy ω is calculated as follows:

$$\hat{G}_{N_0,N_0}(\omega) = \hat{g}_{N_0,N_0}(\omega) + \hat{g}_{N_0,N_0}(\omega)\hat{\Sigma}^{(1)}_{N_0,S}\hat{G}_{S,N_0}(\omega) \tag{24}$$

$$= \hat{g}_{N_0,N_0}(\omega) + \hat{g}_{N_0,N_0}(\omega)\hat{\Sigma}^{(1)}_{N_0,S}\hat{g}_{S,S}(\omega) \times \hat{\Sigma}^{(1)}_{S,N_0}\hat{G}_{N_0,N_0}(\omega). \tag{25}$$

Equation (25) is written as

$$\hat{G}_{N_0,N_0}(\omega) = [\omega - \hat{\Sigma}_{\text{eff}}(\omega)]^{-1}, \tag{26}$$

where, in the large-gap approximation, the effective self-energy $\hat{\Sigma}_{\text{eff}}(\omega)$ given by Eqs. (20) and (21) takes the form of the energy-ω independent Hamiltonian $\hat{\mathscr{H}}_{\text{eff}}$ given by Eq. (23), as it was obtained from this compact Green's function calculation.

Superconducting Green's functions. Now, we provide the expression of the superconducting Green's function $\hat{g}_{S_p,S_p}$ appearing in Eq. (23), and we specifically demonstrate that $\hat{g}_{S_p,S_p}(\omega) \equiv \hat{g}_{S_p,S_p}$ is independent of the energy ω. The advanced local superconducting Green's function of lead S_p takes the following form in the presence of a finite gap:

$$\hat{g}_{S_p,S_p}(\omega) = \frac{1}{W\sqrt{|\Delta|^2 - (\omega - i\eta)^2}} \begin{pmatrix} -\omega & |\Delta|e^{i\varphi_p} \\ |\Delta|e^{-i\varphi_p} & -\omega \end{pmatrix}, \tag{27}$$

where η is a small linewidth broadening, i.e., the so-called Dynes parameter [77–80]. Equation (27) can be found in many papers. For instance, this Eq. (27) is the starting point of the current-voltage characteristics calculations in voltage-biased superconducting weak links [81].

The following is obtained in the large-gap approximation:

$$\hat{g}_{S_p,S_p} = \frac{1}{W}\begin{pmatrix} 0 & e^{i\varphi_p} \\ e^{-i\varphi_p} & 0 \end{pmatrix}, \qquad (28)$$

where Eq. (28) is energy independent, as anticipated in the above discussion. Equation (28) is next inserted into the expression (23) of the large-gap Hamiltonian, which is next numerically treated with exact diagonalizations.

C. Boundary conditions

In this subsection, we discuss how the large-gap Hamiltonian given by Eq. (23) is modified in the presence of a finite value for the magnetic field applied perpendicularly to the two-dimensional structure. In the presence of a vector potential $\mathbf{A}$, we make the substitution $\mathbf{p} \to \mathbf{p} + e\mathbf{A}$ for the momentum, and $\mathbf{j} \to (e\hbar/m)[\nabla\varphi + (2e/\hbar)\mathbf{A}]$ for the supercurrent $\mathbf{j}$, where φ denotes the superconducting phase variable. The vector potential is expressed in the gauge $A_x = -By/2$ and $A_y = Bx/2$, where B is the magnetic field.

Now, we calculate how a Cooper pair crosses the left contact from the superconductor S_L at coordinates $(x = x_L - a_0,\ y)$ to the corresponding tight-binding site at $(x = x_L,\ y)$ in the normal metal. Considering first the left superconductor, we implement $\nabla_y\varphi + (2e/\hbar)A_y = 0$ along the S_L-N_0 interface, leading to

$$\varphi_y = -\frac{B(x_L - a_0)y}{\Phi_0'} + \varphi_L^{(0)}, \qquad (29)$$

where $\Phi_0' = \hbar/e = \Phi_0/2\pi$, with $\Phi_0 = h/e$ the superconducting flux quantum. In the second step, we integrate the phase gradient $\nabla\varphi + (2e/\hbar)\mathbf{A}$ in the horizontal direction across the S_L-N_0 interface:

$$\int_{x_L}^{x_L - a_0}\left(\nabla\varphi + \frac{2e}{\hbar}\mathbf{A}\right)\cdot d\mathbf{s} = \frac{Bya_0}{\Phi_0'} + \varphi_y. \qquad (30)$$

Overall, we deduce the phase

$$\varphi_L^{(0)} - \frac{Byx_L}{\Phi_0'} + \frac{2Bya_0}{\Phi_0'}, \qquad (31)$$

where $\varphi_L^{(0)}$ is the superconducting phase variable of the left superconductor. The following self-energy is then included in the normal-metal Hamiltonian on the left-hand side of the rectangular tight-binding lattice, i.e., at coordinate $(x = x_L,\ y)$:

$$\Gamma_{\mathrm{loc}}^{(\mathrm{Left})}(y) = -\frac{(\Sigma^{(1)})^2}{W} e^{i\varphi_L^{(0)}} e^{-iByx_L/\Phi_0'} e^{2iBya_0/\Phi_0'}, \qquad (32)$$

where $\Gamma_{\mathrm{loc}}^{(\mathrm{Left})}(y)$ denotes the electron-hole Nambu component. Similarly, we deduce the following for the right, top, and bottom self-energies along the edges $x = x_R$, $y = y_T$, and $y = y_B$ of the rectangle, respectively:

$$\Gamma_{\mathrm{loc}}^{(\mathrm{Right})}(y) = -\frac{(\Sigma^{(1)})^2}{W} e^{i\varphi_R^{(0)}} e^{-iByx_R/\Phi_0'} e^{-2iBya_0/\Phi_0'}, \qquad (33)$$

$$\Gamma_{\mathrm{loc}}^{(\mathrm{Top})}(x) = -\frac{(\Sigma^{(1)})^2}{W} e^{i\varphi_T^{(0)}} e^{iBxy_T/\Phi_0'} e^{2iBxa_0/\Phi_0'}, \qquad (34)$$

$$\Gamma_{\mathrm{loc}}^{(\mathrm{Bottom})}(x) = -\frac{(\Sigma^{(1)})^2}{W} e^{i\varphi_B^{(0)}} e^{iBxy_B/\Phi_0'} e^{-2iBxa_0/\Phi_0'}. \qquad (35)$$

D. Algorithm

The numerical calculations proceed with exact diagonalizations of the large-gap Hamiltonian defined in the above Secs. II A, II B, and II C. The supercurrents are obtained from the derivative of the ground state energy with respect to the superconducting phase variables. We denote by $\mathscr{E}_0(B, \varphi_1, \ldots, \varphi_n)$ the ground state energy:

$$\mathscr{E}_0(B, \varphi_1, \ldots, \varphi_n) = \sum_\alpha \epsilon_\alpha(B, \varphi_1, \ldots, \varphi_n)\theta[-\epsilon_\alpha(B, \varphi_1, \ldots, \varphi_n)], \qquad (36)$$

where the ABS have the energies $\epsilon_\alpha(B, \varphi_1, \ldots, \varphi_n)$ and the Heaviside θ function selects negative energies in the zero-temperature limit. The current through lead S_p is then given by

$$I_{S_p}(B, \varphi_1, \ldots, \varphi_n) = -\frac{2e}{\hbar}\frac{\partial\mathscr{E}_0}{\partial\varphi_p}(B, \varphi_1, \ldots, \varphi_n). \qquad (37)$$

We next impose the constraint of vanishingly small supercurrent transmitted into the superconducting mirrors, and evaluate the critical current as the maximum over the remaining superconducting phase variables.

E. Further physical remarks on the large-gap approximation

We note that the large-gap approximation becomes exact only at low energy and/or long distance in highly transparent superconductor–normal-metal–superconductor junctions [82–84]. As is often the case in physics, we extend the large-gap calculations to all energy scales, not only considering the low energies at which the approximation is exact.

The coherence length ξ_0 in the large gap approximation is comparable to the Fermi wavelength λ_F, i.e., a few lattice spacings. The summation in Eq. (36) runs over the entire spectrum of ABS, thus addressing all the length scales in comparison with $\xi_0 \approx \lambda_F$.

The large-gap approximation fulfills the requirements of qualitatively capturing the supercurrent transmitted at long distance in the two-, three-, or four-terminal configurations, as well as supercurrent lines between the lateral and the top or bottom superconductors transmitted over the short range $\xi_0 \approx \lambda_F$ at the four corners of the normal-metallic rectangle. To summarize, we consider the large-gap approximation as an operational tool for capturing the qualitative behavior of those multiterminal Josephson junctions.

III. RESULTS

In this section, we present and physically discuss the numerical results obtained from the superconducting tight-binding model presented in the above Sec. II. Our main numerical results are presented in Figs. 2(a), 2(b), 3(c), 3(d), 4(e), and 4(f), corresponding to the full range of the aspect ratios. The corresponding device dimensions are $N \times M = 2\times100$, 5×40, 10×20, 20×10, 40×5, and 100×2 respectively, with the fixed overall tight-binding lattice area $\mathscr{S} = 200\,a_0^2$. The devices geometry ranges from being elongated in the vertical direction to being elongated horizontal direction. The presentation of the results may look unusual in the sense that the discussion in the text proceeds with two

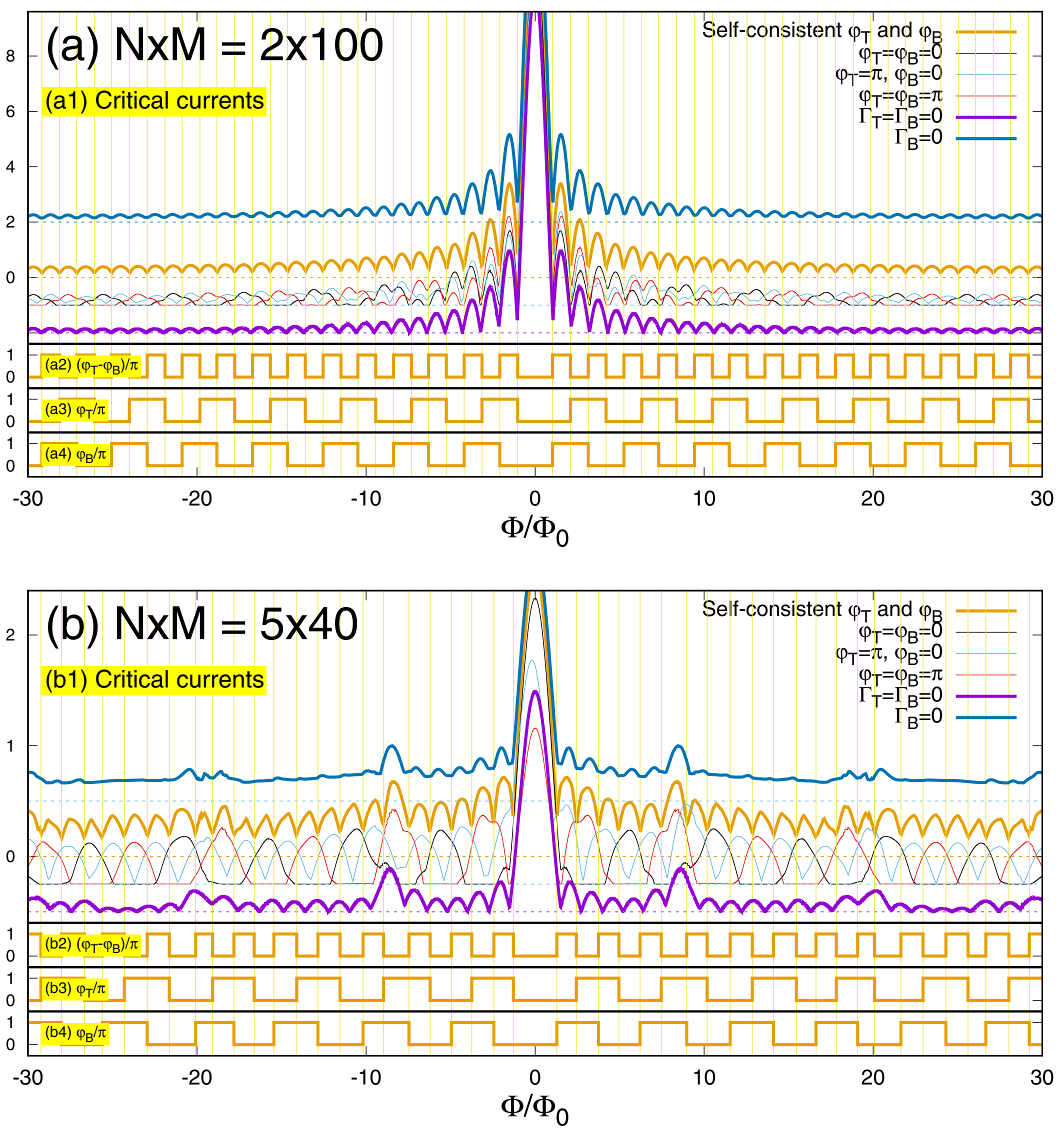

FIG. 2. The numerical results. The critical currents are shown as a function of the reduced magnetic flux, for the self-consistent solution (bold orange lines), and for the non-self-consistent $\varphi_T = \varphi_B = 0$ (thin black lines) and $\varphi_T = \pi$, $\varphi_B = 0$ (light blue lines). The thick magenta lines correspond to absence of coupling to the superconducting leads S_T and S_B on top and bottom, i.e., to a two-terminal Josephson junction with $\Sigma_B^{(1)} = \Sigma_T^{(1)} = 0$. The thick blue lines show a three-terminal Josephson junction having an additional superconducting mirror, with $\Sigma_B^{(1)} = 0$. Panels (a2), (a3), and (a4) show the self-consistent $(\varphi_T - \varphi_B)/\pi$, φ_T/π, and φ_B/π respectively with two superconducting mirrors. We use $\Sigma_0 = 10$ for the bulk hopping amplitude in N_0, $\Gamma_L = \Gamma_R = \Gamma_T = \Gamma_B \equiv \Gamma$ with $\Gamma = 1$ for the contact transparencies, and $W_g = 0.4$ for the value of the gate voltage. The supercurrents are in units of $2e\Gamma/\hbar$. We also use $N\times M = 2\times 100$ [panel (a)] and $N\times M = 5\times 40$ [panel (b)]. Panel (a) shows oscillating critical current with $N \ll M$, i.e., with $N = 2$ and $M = 100$. Then, the magnetic oscillations resemble a Fraunhofer pattern. Panel (b) shows the evolution of the oscillating patterns for the smaller aspect ratio $N = 5$ and $M = 40$.

terminals, then two terminals plus a single superconducting mirror, and finally two terminals plus two superconducting mirrors, thus not consisting of a discussion of the figures one after the other.

Regarding the size of the numerically implemented rectangular lattices, we obtained a crossover to the semiclassical spectra [82–84] for larger dimensions, typically 100×200 or 100×400 lattices (those data are not shown as figures in the present paper). However, the multiterminal effects that we consider do not rely on whether the semiclassical limit is fully realized. This is why we address here intermediate device dimensions at reduced computational expanses. The area is sufficient to produce viable numerical data for the critical current as a function of the magnetic field.

Concerning the devices containing a single or two superconducting mirrors, considerable gains in the computation times are obtained if all of the superconducting leads S_L, S_R, S_T, and S_B are coupled to the normal-metallic conductor N_0 by symmetric hopping amplitudes; see the Appendix. This symmetry condition is fulfilled by the identical hopping amplitudes implemented in our calculations.

After recovering known behavior with two terminals, the numerical results with superconducting mirrors will next be presented and discussed. The supercurrent flowing between

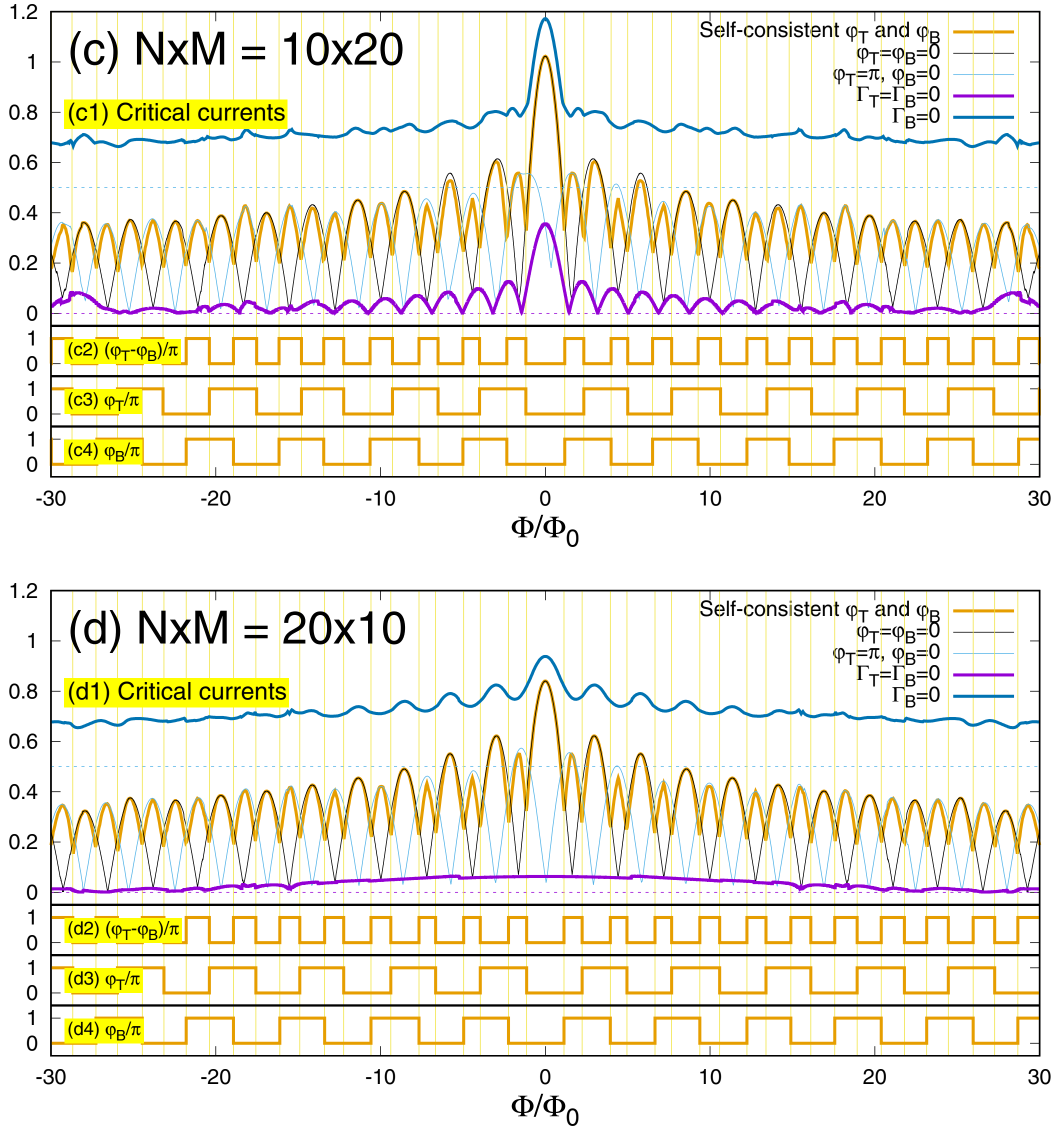

FIG. 3. The same as Fig. 2 but now with $N\times M = 10\times 20$ [panel (c)] and $N\times M = 20\times 10$ [panel (d)]. Panels (c) and (d) show the crossover from *elongated along the y-axis direction* [panel (c)] to *elongated along the x-axis direction* [panel (d)]. With two terminals, panel (c) shows an oscillation pattern while panel (d) features quasimonotonic decay of the critical current as a function of the magnetic field. In addition, the four-terminal critical current oscillation patterns resemble those a SQUID in panels (c) and (d).

the left and right superconductors S_L and S_R in the horizontal direction will be enhanced by orders of magnitudes in the presence of the single superconducting mirror S_T. With the two superconducting mirrors S_T and S_B, we will obtain an oscillatory critical current magnetic pattern that resembles the oscillations of a SQUID, due to the interfering supercurrent paths through the top and bottom superconductors S_T and S_B.

Two terminals. Now, we proceed with discussing the numerical results themselves, starting with two terminals as a point of comparison for testing the large-gap calculations. We first consider a device where the two superconducting leads S_L and S_R are connected to the left and right, with the superconducting mirrors S_T and S_B neither on top nor on bottom [see Figs. 1(a) and 1(b)]. The numerical data with two terminals are shown with the bold magenta lines labeled by $\Gamma_T = \Gamma_B = 0$ in panels (a1)–(f1) of Figs. 2–4.

Figures 2(a), 2(b), and 3(c) correspond to $N\times M = 2\times 100$, $N\times M = 5\times 40$, and $N\times M = 10\times 20$ respectively. We then obtain the expected Fraunhofer-like oscillation pattern for those devices elongated along the y-axis direction.

Next, the two-terminal critical current is negligibly small if the device is elongated along the x-axis direction; see the bold magenta lines labeled by $\Gamma_T = \Gamma_B = 0$ in Figs. 4(e) and 4(f) with $N\times M = 40\times 5$ and $N\times M = 100\times 2$ respectively.

We also find quasimonotonic decay of the critical current as a function of the magnetic field if the device dimension in the horizontal direction is reduced according to $N\times M = 20\times 10$; see the bold magenta line in Fig. 3(d). We carried out complementary calculations of the ABS spectrum, revealing that the small "jumps" appearing in the data points represented by the bold magenta lines in Fig. 3(d) signal that some ABS cross the zero of energy as a function of the magnetic field.

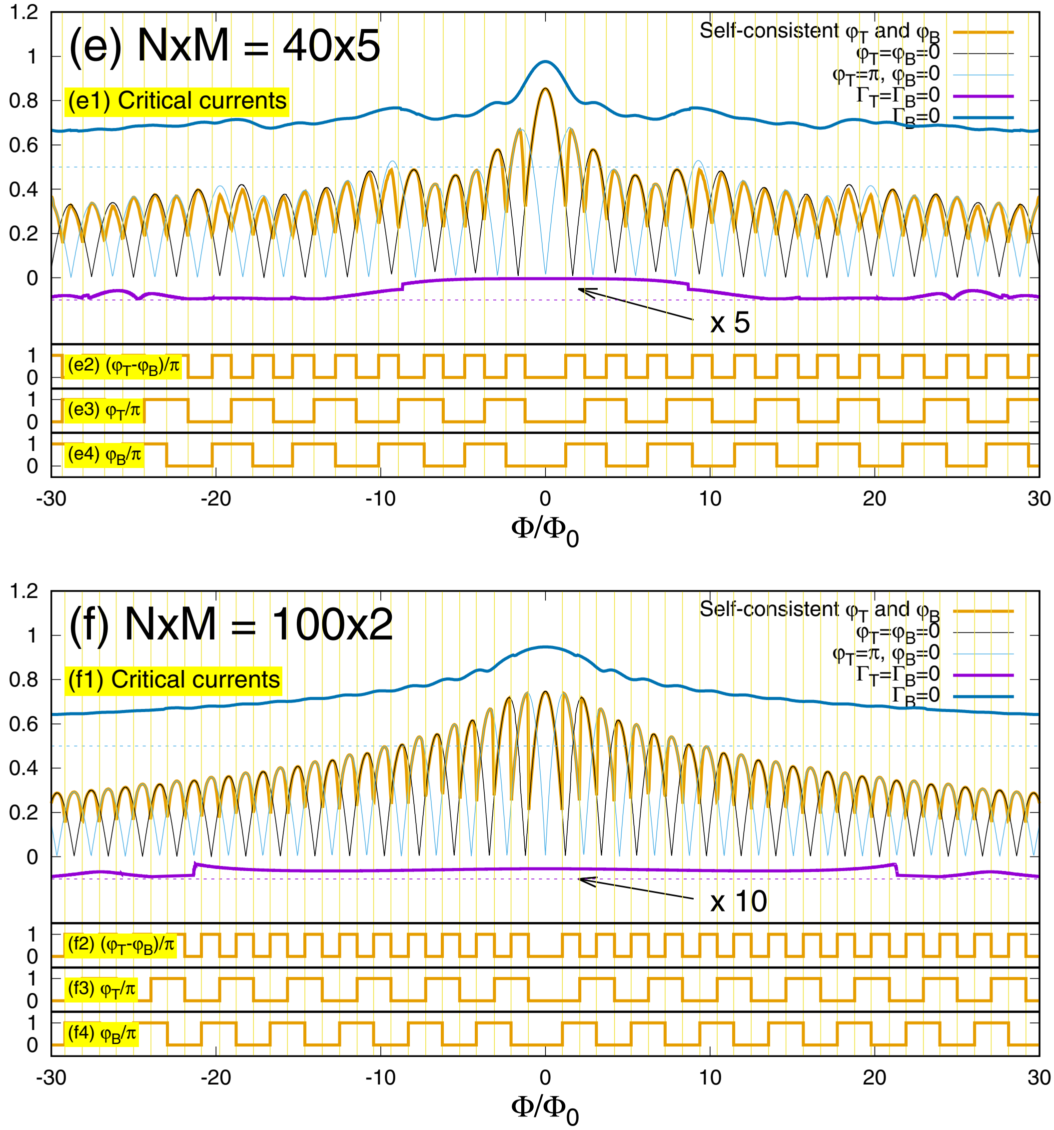

FIG. 4. The same as Fig. 2 but, in addition, the thin red lines correspond to $\varphi_T = \varphi_B = \pi$. We use $N\times M = 40\times5$ [panel (e)] and $N\times M = 100\times2$ [panel (f)]. The figure shows aspect ratios strongly elongated along the x-axis direction, i.e., with $N \gg M$. Then, the two-terminal oscillation patterns reveal negligibly small signal, and the four-terminal ones show the SQUID-like oscillations coexisting with the long-range effect of the superconducting mirrors.

The overall evolution from Fraunhofer pattern to quasi-monotonic decay of the critical current flowing from S_L to S_R is in qualitative agreement with a preceding work on disordered superconductor–normal-metal–superconductor junctions in a field; see Ref. [85]. Now that we demonstrated consistency with known results, we further proceed with three- and four-terminal devices containing a single or two superconducting mirrors respectively.

A single superconducting mirror. Now we consider that a third superconducting lead S_T is connected on top to the rectangular normal-metallic conductor N_0; see Fig. 1(c). We calculate the maximal value of the supercurrent flowing between S_L and S_R connected to the left and right edges respectively. As discussed above, S_T on top is an open-circuit superconducting mirror and the overall supercurrent transmitted into S_T is vanishingly small. However, S_T can propagate supercurrent in the direction parallel to its interface with N_0.

The corresponding data for the critical current in the presence of this third superconducting mirror S_T laterally connected on top are shown by the dark blue lines labeled by $\Gamma_B = 0$ in Figs. 2(a1) to 4(f1). Those datapoints are vertically shifted according to the reference represented by the horizontal blue dashed lines.

Devices elongated in the vertical direction produce oscillations in the critical current as a function of the applied magnetic field; see the dark blue lines in Figs. 2(a1) to 3(d1) corresponding to $N\times M = 2\times100$, 5×40, 10×20, 20×10 respectively. We note that, for those device dimensions, the ratio between the critical currents at the central peak and at the first lobe is anomalously large in comparison with the standard Fraunhofer pattern [60]. Given the intermediate contact transparencies in our calculations, we possibly relate this zero-field anomaly to the constructive interference of reflectionless tunneling at low magnetic field; see Ref. [86].

The corresponding critical currents flowing between the left and right superconductors S_L and S_R in the horizontal direction are shown by the dark blue lines labeled by $\Gamma_B = 0$ in panels (e1)–(f1) of Fig. 4, for $N\times M = 40\times 5$ and $N\times M = 100\times 2$. Those values are enhanced by orders or magnitude in comparison with a two-terminal device (i.e., with $\Gamma_T = \Gamma_B = 0$ in the absence of the coupling to S_T). This enhancement is interpreted as phase rigidity in the superconductor mirror S_T connected on top. Namely, propagating supercurrent from S_L to S_R in the horizontal direction involves supercurrent lines connecting S_L to S_T, followed by propagation over arbitrary long distances inside the rigid condensate of S_T, and finally the supercurrent lines are transmitted from S_T to S_R.

Two superconducting mirrors. We now consider the four-terminal Josephson device with two superconducting mirrors, where the supercurrent in the horizontal direction flows between the two superconductors S_L and S_R connected to the left and right edges of the rectangular normal-metallic N_0, in the presence of the two superconducting mirrors S_T and S_B laterally connected on top and bottom; see Figs. 1(d) and 1(e).

Panels (a1)–(f1) of Figs. 2–4 show the critical currents as a function of the magnetic field, with self-consistent superconducting phase variables (see the bold orange lines labeled by "Self-consistent φ_T and φ_B"). The self-consistent solution minimizes the ground state energy $\mathscr{E}_0$ with respect to the superconducting phase variables $\varphi_T, \varphi_B = 0$ or π according to the Appendix; see also Eq. (36) for the expression of the ground state energy $\mathscr{E}_0$.

As for a single superconducting mirror S_T, we observe that connecting the two superconducting mirrors S_T and S_B on top and bottom produces an enhancement of the critical current flowing between the left and right superconductors S_L and S_R in the horizontal direction; see Figs. 4(a) and 4(b) for $N\times M = 40\times 5$ and $N\times M = 100\times 2$ respectively. The supercurrent from S_L and S_R or from S_R to S_L in the horizontal direction can be viewed as being *guided* by the superconducting mirrors S_T and S_B on top and bottom.

The critical current magnetic oscillations resemble those of a SQUID, due to the interference between the Cooper pairs traveling in the superconducting leads S_T and S_B on top and bottom respectively.

The thinner black lines labeled by "$\varphi_T = \varphi_B = 0$" in Figs. 2(a), 2(b), 3(c), 3(d), 4(e), and 4(f) show the critical current with the non-self-consistent $\varphi_T = \varphi_B = 0$, and the thinner light-blue lines labeled by "$\varphi_T = \pi$, $\varphi_B = 0$" correspond to the non-self-consistent $\varphi_T = \pi$ and $\varphi_B = 0$. The light-red lines labeled by "$\varphi_T = \varphi_B = \pi$" in Figs. 2(a) and 2(b) correspond to $\varphi_T = \varphi_B = \pi$. We conclude that the critical current calculated with the self-consistent φ_T and φ_B (see the bold orange lines labeled by "Self-consistent φ_T and φ_B") switches between those non-self-consistent solutions as the magnetic field is increased.

Figures 2(a2) to 4(f2) show the normalized difference $(\varphi_T - \varphi_B)/\pi$ between the self-consistent phase variables φ_T and φ_B of the superconducting mirrors. Figures 2(a3) to 4(f3) and Figs. 2(a4) to 4(f4) show the normalized self-consistent φ_T/π and φ_B/π respectively. Remarkably, all minima in the critical current pattern in panels (a1)–(f1) correlate with the magnetic field values at which $(\varphi_T - \varphi_B)/\pi$ switches between zero and unity or vice versa. The thin vertical yellow lines across each of Figs. 2–4 match all of those switching points in $(\varphi_T - \varphi_B)/\pi$.

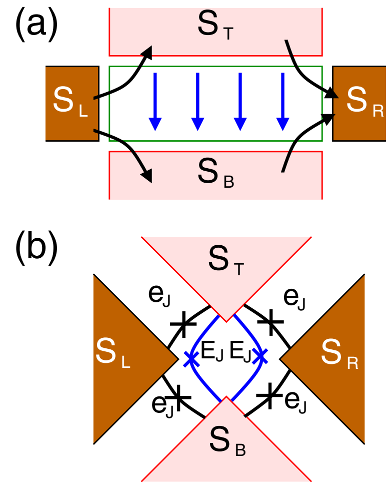

FIG. 5. The four superconducting leads S_L, S_R, S_T, and S_B on the left, right, top, and bottom (a) are transformed into the phenomenological Josephson junction circuit model (b). The neighboring superconducting leads are connected by *small* Josephson coupling e_J and the top and bottom ones S_T and S_B are connected by two Josephson junctions with *large* Josephson coupling E_J, reflecting the corresponding large-area contacts between S_T and S_B through the normal metal N_0.

We conclude that, in the limit of a device elongated in the horizontal direction (i.e., with $N \gg M$), the magnetic field dependence of the critical current is controlled by $(\varphi_T - \varphi_B)/\pi$, instead of each φ_T/π or φ_B/π taken individually. In the opposite limit of a device elongated in the vertical direction (i.e., if $M \gg N$), the superconducting phase variables φ_T and φ_B of S_T and S_B are *spectators*. Their values are driven by the supercurrent flowing between S_L and S_R in the horizontal direction. In addition, Figs. 2(a) and 2(b) feature the magnetic flux dependence of the non-self-consistent $\varphi_T = \varphi_B = \pi$, which strongly deviates from the non-self-consistent $\varphi_T = \varphi_B = 0$.

IV. PHENOMENOLOGICAL JOSEPHSON JUNCTION CIRCUIT MODEL

In this section, we propose a phenomenological Josephson junction circuit model suitable to geometries elongated in the horizontal direction, i.e., with $N \gg M$. The Josephson coupling energy E_J between the top and bottom superconductors S_T and S_B is large, due to the corresponding large area interfaces. The Josephson coupling energies e_J between the pairs (S_B, S_L), (S_L, S_T), (S_T, S_R), and (S_R, S_B) is smaller; see Fig. 5. This simple model relies on a few weak links and it is thus not intended to capture the zero-field anomaly appearing in the above numerical calculations.

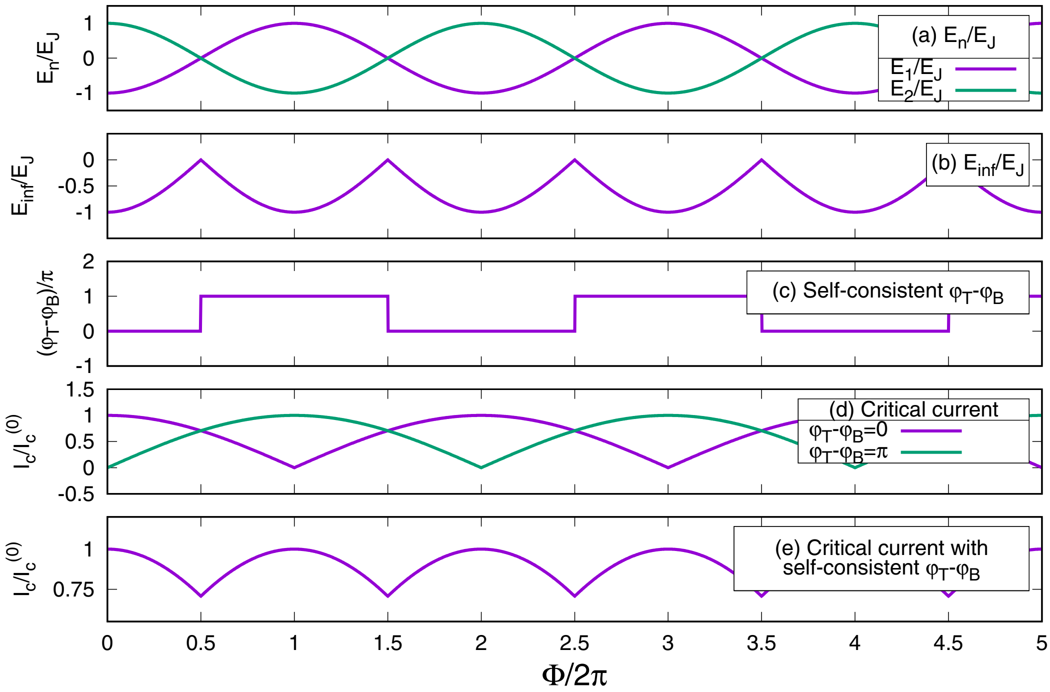

FIG. 6. The figure illustrates the phenomenological Josephson junction circuit model calculation. The figure shows the energies E_1 and E_2 as a function of $\Phi/2\pi$ [see Eq. (40)] (a), the ground state energy $E_{\rm inf} = \inf(E_1, E_2)$ between the lowest between E_1 and E_2 (b), the normalized self-consistent $(\varphi_T - \varphi_B)/2\pi$ (c), the non-self-consistent critical currents I_c for $\varphi_T - \varphi_B = 0$ and $\varphi_T - \varphi_B = \pi$ (d), and the critical current I_c with the self-consistent $\varphi_T - \varphi_B$ (e).

The total energy takes the form

$$\begin{aligned} E =& -E_J \cos\left(\varphi_T - \varphi_B + \frac{\Phi}{2\Phi_0}\right) \\ &- E_J \cos\left(\varphi_T - \varphi_B - \frac{\Phi}{2\Phi_0}\right) \\ &- e_J \cos\left(\varphi_T - \varphi_L + \frac{\Phi}{4\Phi_0}\right) \\ &- e_J \cos\left(\varphi_L - \varphi_B + \frac{\Phi}{4\Phi_0}\right) \\ &- e_J \cos\left(\varphi_B - \varphi_R + \frac{\Phi}{4\Phi_0}\right) \\ &- e_J \cos\left(\varphi_R - \varphi_T + \frac{\Phi}{4\Phi_0}\right). \end{aligned} \quad (38)$$

Assuming $E_J \gg e_J$, the supercurrent entering S_T is approximated as

$$\begin{aligned} -\frac{2e}{\hbar}\frac{\partial E}{\partial \varphi_T} \simeq& \frac{2e}{\hbar} E_J \sin\left(\varphi_T - \varphi_B + \frac{\Phi}{2\Phi_0}\right) \\ &+ \frac{2e}{\hbar} E_J \sin\left(\varphi_T - \varphi_B - \frac{\Phi}{2\Phi_0}\right). \end{aligned} \quad (39)$$

Injecting $\varphi_T - \varphi_B = 0$ or π into Eq. (39) leads to the zero-current condition $-(2e/\hbar)\partial E/\partial\varphi_T = 0$, with the corresponding energies E_1 and E_2,

$$E_1 = -2E_J \cos\left(\frac{\Phi}{2\Phi_0}\right) \equiv -E_2, \quad (40)$$

associated with $\varphi_T - \varphi_B = 0$ and $\varphi_T - \varphi_B = \pi$ respectively. As the normalized magnetic flux Φ/Φ_0 increases, the ground state energy alternates between E_1 and E_2 in Eq. (40), corresponding to locking the phases φ_T and φ_B according to $\varphi_T - \varphi_B = 0$ or $\varphi_T - \varphi_B = \pi$ respectively. For instance, $\varphi_T - \varphi_B = 0$ and $\varphi_T - \varphi_B = \pi$ are obtained in the intervals $|\Phi/2\Phi_0| < \pi/2$ and $\pi/2 < |\Phi/2\Phi_0| < 3\pi/2$ respectively.

Figures 6(a) to 6(c) illustrate the flux-sensitivity of E_1, E_2 in Eq. (40) [panel (a)], the ground state energy $E_{\rm inf} = \inf(E_1, E_2)$ [panel (b)], and the self-consistent $\varphi_T - \varphi_B$ [panel (c)]. Comments on panels (d) and (e) are provided below.

Now, we successively evaluate the supercurrents for $\varphi_T - \varphi_B = 0$ and $\varphi_T - \varphi_B = \pi$. First considering $\varphi_T = \varphi_B = 0$ leads to the following expression of the φ_L- and φ_R-sensitive energy terms E_L and E_R:

$$\begin{aligned} E_L(\varphi_L, \Phi) =& -e_J \cos\left(-\varphi_L + \frac{\Phi}{4\Phi_0}\right) \\ &- e_J \cos\left(\varphi_L + \frac{\Phi}{4\Phi_0}\right) \quad (41) \\ =& -2e_J \cos\varphi_L \cos\left(\frac{\Phi}{4\Phi_0}\right), \quad (42) \end{aligned}$$

$$\begin{aligned} E_R(\varphi_R, \Phi) =& -e_J \cos\left(-\varphi_R + \frac{\Phi}{4\Phi_0}\right) \\ &- e_J \cos\left(\varphi_R + \frac{\Phi}{4\Phi_0}\right) \quad (43) \\ =& -2e_J \cos\varphi_R \cos\left(\frac{\Phi}{4\Phi_0}\right). \quad (44) \end{aligned}$$

We obtain

$$I_L(\varphi_L,\Phi) = -\frac{2e}{\hbar}\frac{\partial E_L}{\partial \varphi_L}(\varphi_L,\Phi) \quad (45)$$

$$= -\frac{4e}{\hbar}e_J \sin\varphi_L \cos\left(\frac{\Phi}{4\Phi_0}\right), \quad (46)$$

$$I_R(\varphi_R,\Phi) = -\frac{2e}{\hbar}\frac{\partial E_R}{\partial \varphi_R}(\varphi_R,\Phi) \quad (47)$$

$$= -\frac{4e}{\hbar}e_J \sin\varphi_R \cos\left(\frac{\Phi}{4\Phi_0}\right). \quad (48)$$

The condition $I_R + I_L = 0$ leads to $\sin\varphi_L = -\sin\varphi_R$, and to $\varphi_R = -\varphi_L$ or $\varphi_R = \varphi_L + \pi$. We observe that $E_L(\varphi_L,\Phi) + E_R(\varphi_L + \pi,\Phi) = 0$, and we can always find values of φ_L having the lower energy $E_L(\varphi_L,\Phi) + E_R(-\varphi_L,\Phi) < 0$, which is why we restrict to $\varphi_R = -\varphi_L \equiv \psi$. It turns out that the ground state energy is negative for all values of the reduced magnetic flux Φ/Φ_0; see Fig. 6(b).

Assuming now $\varphi_T = 0$ and $\varphi_B = \pi$, we obtain

$$E'_L(\varphi_L,\Phi) = -e_J\cos\left(-\varphi_L + \frac{\Phi}{4\Phi_0}\right)$$

$$+ e_J\cos\left(\varphi_L + \frac{\Phi}{4\Phi_0}\right) \quad (49)$$

$$= -2e_J \sin\varphi_L \sin\left(\frac{\Phi}{4\Phi_0}\right), \quad (50)$$

$$E'_R(\varphi_R,\Phi) = e_J\cos\left(-\varphi_R + \frac{\Phi}{4\Phi_0}\right)$$

$$- e_J\cos\left(\varphi_R + \frac{\Phi}{4\Phi_0}\right) \quad (51)$$

$$= 2e_J \sin\varphi_R \sin\left(\frac{\Phi}{4\Phi_0}\right), \quad (52)$$

and

$$I'_L(\varphi_L,\Phi) = -\frac{2e}{\hbar}\frac{\partial E'_L}{\partial \varphi_L}(\varphi_L,\Phi) \quad (53)$$

$$= \frac{4e}{\hbar}e_J \cos\varphi_L \sin\left(\frac{\Phi}{4\Phi_0}\right), \quad (54)$$

$$I'_R(\varphi_R,\Phi) = -\frac{2e}{\hbar}\frac{\partial E'_R}{\partial \varphi_R}(\varphi_R,\Phi) \quad (55)$$

$$= -\frac{4e}{\hbar}e_J \cos\varphi_R \sin\left(\frac{\Phi}{4\Phi_0}\right), \quad (56)$$

where, again, we used $\varphi_R = -\varphi_L \equiv \psi$.

Figure 6(d) shows the critical current as a function of the normalized magnetic flux for the non-self-consistent solutions with $\varphi_T - \varphi_B = 0$ and $\varphi_T - \varphi_B = \pi$. Figure 6(e) shows the value of the supercurrent calculated with the self-consistent $\varphi_T - \varphi_B$, which amounts to taking the maximum between the two values on Fig. 6(d). We note consistency with the preceding numerical calculations presented in Figs. 2–4; see the above Sec. III.

Finally, we have four phase variables φ_L, φ_R, φ_T, and φ_B. The constraint $\varphi_R = -\varphi_L \equiv \psi$ originates from the external current source which imposes opposite supercurrents transmitted into S_L and S_R, therefore defining a net current flowing from S_L to S_R or from S_R to S_L in the horizontal direction. Those opposite supercurrents $I_R = -I_L$ couple to the remaining phase combinations $\varphi_T - \varphi_B = 0$ or π and $\varphi_R = -\varphi_L \equiv \psi$, where φ_B is left undetermined. This is compatible with gauge invariance where one of those superconducting phase variables cannot be fixed. We conclude that, if $N \gg M$, the supercurrent flowing from S_L to S_R or from S_R to S_L in the horizontal direction couples to all possibly allowed phase combinations, as is already the case in the short-junction limit.

V. CONCLUSIONS

To conclude, we considered a multiterminal Josephson junction circuit model with the four superconducting leads S_L, S_R, S_T, and S_B connected to the left, right, top, and bottom edges of a normal-metallic rectangle N_0.

Concerning three terminals, we demonstrated that, for devices elongated in the horizontal direction, attaching the superconducting mirror S_T on top of the normal conductor N_0 enhances the horizontal supercurrent by orders of magnitude, as a result of phase rigidity in the open-circuit superconductor S_T.

Concerning four terminals, we calculated the supercurrent flowing from S_L to S_R in the horizontal direction in the presence of the two superconducting mirrors S_T and S_B, and we obtained oscillatory magnetic oscillations reminiscent of a SQUID. Those oscillations are controlled by the self-consistent phase variables φ_T and φ_B of the superconductors S_T and S_B connected on top and bottom respectively.

If the hopping amplitudes connecting the ballistic rectangular normal-metallic conductor N_0 to the superconductors are symmetric, then φ_T and φ_B take the values 0 or π, as for an emerging Ising degree of freedom.

We also interpreted our numerical results with a simple Josephson junction circuit model, and demonstrated that the supercurrent flows through all parts of the circuit if the device is elongated in the horizontal direction.

In the numerical calculations and in the phenomenological circuit model, the horizontal supercurrent was controlled by the difference $\varphi_T - \varphi_B = 0$ or π instead of each individual φ_T or φ_B, thus providing sensitivity to a single effective Ising degree of freedom of the supercurrent flowing in the horizontal direction.

Finally, a long-range effect was reported in the experimental results of Ref. [55] and is compatible with our theory of the superconducting mirrors. In addition, a recent experimental work [49] measured the critical current contours (CCCs) in the plane of the two biasing currents I_1 and I_2. The zero-current conditions $I_1 = 0$ or $I_2 = 0$ are fulfilled at the points where the CCCs intersect the x- or y-current axis respectively. Thus, our theory of the phase rigidity is expected to produce specific signatures on the CCCs, which will be the subject of a future work. Perspectives also include generalization to Josephson junction arrays [48,51,87–89].

ACKNOWLEDGMENTS

The authors benefited from fruitful discussions with M. d'Astuto, D. Beckmann, J. G. Caputo, H. Cercellier, I. Gornyi, T. Klein, F. Lévy-Bertrand, M. A. Méasson, and P.

Rodière. R.M. thanks the Infrastructure de Calcul Intensif et de Données (GRICAD) for use of the resources of the Mésocentre de Calcul Intensif de l'Université Grenoble-Alpes (CIMENT). This work was supported by the International Research Project SUPRADEVMAT between CNRS in Grenoble and KIT in Karlsruhe. This work received support from the French National Research Agency (ANR) in the framework of the Graphmon project (ANR-19-CE47-0007). This work was partly supported by Helmholtz Society through program NACIP and the DFG via the Project No. DA 1280/7-1.

APPENDIX: SYMMETRIES

In this Appendix, we show how the symmetries considerably reduce the computation times if the current flowing from S_L to S_R in the horizontal direction is specifically evaluated. Namely, we demonstrate that the symmetries

$$\varphi_T, \varphi_B = 0 \text{ or } \pi \quad \text{and} \quad \varphi_L = -\varphi_R \equiv \psi \tag{A1}$$

are equivalent to vanishingly small supercurrent transmitted into the top and bottom superconductors S_T and S_B; i.e., (A1) implies that S_T and S_B are superconducting mirrors. The condition (A1) also implies that opposite supercurrents are transmitted into S_L and S_R connected on the left and right edges of the rectangular normal-metallic conductor N_0. Conservation of the supercurrent between S_L and S_R in the horizontal direction is thus automatically fulfilled. Now, we demonstrate those statements.

Equations (32) and (33) become

$$\Gamma^{(\text{Left})}_{\text{loc}}(y) = -\frac{(\Sigma^{(1)})^2}{W} e^{i\varphi_L^{(0)}} e^{iBLy/2\Phi_0'} e^{2iBya_0/\Phi_0'}, \tag{A2}$$

$$\Gamma^{(\text{Right})}_{\text{loc}}(y) = -\frac{(\Sigma^{(1)})^2}{W} e^{i\varphi_R^{(0)}} e^{-iBLy/2\Phi_0'} e^{-2iBya_0/\Phi_0'}, \tag{A3}$$

where we use the notation $x_{R/L} = \pm L/2$. We obtain

$$\Gamma^{(\text{Left})}_{\text{loc}}(y) = \left(\Gamma^{(\text{Right})}_{\text{loc}}\right)^*(y) \tag{A4}$$

if $e^{i\varphi_L^{(0)}} = e^{-i\varphi_R^{(0)}}$, i.e., if $\varphi_L = -\varphi_R \equiv \psi$; see the condition (A1).

Conversely, the substitution $x \to \tilde{x} = -x$ leads to $\Gamma^{(\text{Top})}_{\text{loc}} \to \tilde{\Gamma}^{(\text{Top})}_{\text{loc}}$ and $\Gamma^{(\text{Bottom})}_{\text{loc}} \to \tilde{\Gamma}^{(\text{Bottom})}_{\text{loc}}$ in Eqs. (34) and (35), with

$$\tilde{\Gamma}^{(\text{Top})}_{\text{loc}}(x) = -\frac{(\Sigma^{(1)})^2}{W} e^{i\varphi_T^{(0)}} e^{-iBWx/2\Phi_0'} e^{-2iBxa_0/\Phi_0'}, \tag{A5}$$

$$\tilde{\Gamma}^{(\text{Bottom})}_{\text{loc}}(x) = -\frac{(\Sigma^{(1)})^2}{W} e^{i\varphi_B^{(0)}} e^{iBWx/2\Phi_0'} e^{2iBxa_0/\Phi_0'}, \tag{A6}$$

where we used the notation $y_{T,B} = \pm W/2$.

We deduce the following:

$$\tilde{\Gamma}^{(\text{Top})}_{\text{loc}} = \left(\Gamma^{(\text{Top})}_{\text{loc}}\right)^*, \tag{A7}$$

$$\tilde{\Gamma}^{(\text{Bottom})}_{\text{loc}} = \left(\Gamma^{(\text{Bottom})}_{\text{loc}}\right)^* \tag{A8}$$

if both $e^{i\varphi_B^{(0)}}$ and $e^{i\varphi_T^{(0)}}$ are real valued, i.e., if $\varphi_B^{(0)}, \varphi_T^{(0)} = 0$ or π; see the condition (A1).

Now, we discuss the consequences for the supercurrents flowing across the normal-metallic conductor N_0. At the lowest order in tunneling, the typical combinations

$$\Gamma^{(\text{Left})}_{\text{loc}}(y)\left(\Gamma^{(\text{Bottom})}_{\text{loc}}(x)\right)^* \tag{A9}$$

and

$$\Gamma^{(\text{Right})}_{\text{loc}}(y)\left(\Gamma^{(\text{Bottom})}_{\text{loc}}(x)\right)^* \tag{A10}$$

control the DC-Josephson effect between the left/bottom and the right/bottom superconducting leads. The identity

$$\Gamma^{(\text{Left})}_{\text{loc}}(y)\left(\Gamma^{(\text{Bottom})}_{\text{loc}}(x)\right)^* = \left[\Gamma^{(\text{Right})}_{\text{loc}}(y)\left(\Gamma^{(\text{Bottom})}_{\text{loc}}(-x)\right)^*\right]^* \tag{A11}$$

leads to opposite values for the supercurrents transmitted from left to bottom and from right to bottom if the condition (A1) is fulfilled, since the corresponding superconducting phase differences are opposite.

We conclude that the mirror-axis symmetry $x \to \tilde{x} = -x$ leads to vanishingly small value for the sum $I_{L\to B} + I_{R\to B}$ of the supercurrents $I_{L\to B}$ (from left to bottom) and $I_{R\to B}$ (from right to bottom), i.e., $I_{L\to B} + I_{R\to B} = 0$. Similarly, we find $I_{L\to T} + I_{R\to T} = 0$ for the sum of the supercurrents from left to top and from right to top.

Using the form of the Bethe-Salpeter equations suitable to Andreev tubes (see for instance Refs. [69,70] for the Andreev tubes), this perturbative argument can be extended to all orders in the tunneling amplitudes $\Sigma^{(1)}$ connecting the normal region N_0 to each of the superconducting leads; see Eq. (5) for the notation $\Sigma^{(1)}$.

In Sec. III of the main text, the three- and four-terminal calculations with a single or two superconducting mirrors respectively are realized with identical value for all of the tunneling amplitudes between the normal region N_0 and the superconductors. The symmetry condition (A1) is then automatically fulfilled and the energy minimum is within the discrete set $\varphi_T, \varphi_B = 0$ or π. Scanning those restricted values of φ_T and φ_B (as it was the case in the above Sec. III) allows for considerable gain in the computation time with respect to looking for the energy minimum in the entire $[0, 2\pi]\times[0, 2\pi]$ intervals.

[1] R. de Bruyn Ouboter and A. Omelyanchouk, Multi-terminal squid controlled by the transport current, Phys. B: Condens. Matter **205**, 153 (1995).

[2] M. H. S. Amin, A. N. Omelyanchouk, and A. M. Zagoskin, Mesoscopic multiterminal Josephson structures. I. Effects of nonlocal weak coupling, Low Temp. Phys. **27**, 616 (2001).

[3] M. H. S. Amin, A. N. Omelyanchouk, and A. M. Zagoskin, DC SQUID based on the mesoscopic multiterminal Josephson junction, Physica C **372-376**, 178 (2002).

[4] M. H. S. Amin, A. N. Omelyanchouk, A. Blais, A. M. van den Brink, G. Rose, T. Duty, and A. Zagoskin, Multi-terminal superconducting phase qubit, Physica C **368**, 310 (2002).

[5] A. Freyn, B. Douçot, D. Feinberg, and R. Mélin, Production of nonlocal quartets and phase-sensitive entanglement in a superconducting beam splitter, Phys. Rev. Lett. **106**, 257005 (2011).
[6] R. Mélin, D. Feinberg, and B. Douçot, Partially resummed perturbation theory for multiple Andreev reflections in a short three-terminal Josephson junction, Eur. Phys. J. B **89**, 67 (2016).
[7] T. Jonckheere, J. Rech, T. Martin, B. Douçot, D. Feinberg, and R. Mélin, Multipair dc Josephson resonances in a biased allsuperconducting bijunction, Phys. Rev. B **87**, 214501 (2013).
[8] R. Mélin, Inversion in a four terminal superconducting device on the quartet line. I. Two-dimensional metal and the quartet beam splitter, Phys. Rev. B **102**, 245435 (2020).
[9] R. Mélin and B. Douçot, Inversion in a four terminal superconducting device on the quartet line. II. Quantum dot and Floquet theory, Phys. Rev. B **102**, 245436 (2020).
[10] R. Mélin and D. Feinberg, Quantum interferometer for quartets in superconducting three-terminal Josephson junctions, Phys. Rev. B **107**, L161405 (2023).
[11] R. Mélin, R. Danneau, and C. B. Winkelmann, Proposal for detecting the π-shifted Cooper quartet supercurrent, Phys. Rev. Res. **5**, 033124 (2023).
[12] R. Mélin, J.-G. Caputo, K. Yang, and B. Douçot, Simple Floquet-Wannier-Stark-Andreev viewpoint and emergence of low-energy scales in a voltage-biased three-terminal Josephson junction, Phys. Rev. B **95**, 085415 (2017).
[13] R. Mélin, R. Danneau, K. Yang, J.-G. Caputo, and B. Douçot, Engineering the Floquet spectrum of superconducting multiterminal quantum dots, Phys. Rev. B **100**, 035450 (2019).
[14] B. Douçot, R. Danneau, K. Yang, J.-G. Caputo, and R. Mélin, Berry phase in superconducting multiterminal quantum dots, Phys. Rev. B **101**, 035411 (2020).
[15] R. Mélin, Ultralong-distance quantum correlations in three-terminal Josephson junctions, Phys. Rev. B **104**, 075402 (2021).
[16] R. Mélin, Multiterminal ballistic Josephson junctions coupled to normal leads, Phys. Rev. B **105**, 155418 (2022).
[17] A. Keliri and B. Douçot, Driven Andreev molecule, Phys. Rev. B **107**, 094505 (2023); Long-range coupling between superconducting dots induced by periodic driving, *ibid.* **108**, 184516 (2023).
[18] R.-P. Riwar, M. Houzet, J. S. Meyer, and Y. V. Nazarov, Multi-terminal Josephson junctions as topological materials, Nat. Commun. **7**, 11167 (2016).
[19] E. Eriksson, R.-P. Riwar, M. Houzet, J. S. Meyer, and Y. V. Nazarov, Topological transconductance quantization in a four-terminal Josephson junction, Phys. Rev. B **95**, 075417 (2017).
[20] H.-Y. Xie, M. G. Vavilov, and A. Levchenko, Topological Andreev bands in three-terminal Josephson junctions, Phys. Rev. B **96**, 161406(R) (2017).
[21] H.-Y. Xie, M. G. Vavilov, and A. Levchenko, Weyl nodes in Andreev spectra of multiterminal Josephson junctions: Chern numbers, conductances, and supercurrents, Phys. Rev. B **97**, 035443 (2018).
[22] O. Deb, K. Sengupta, and D. Sen, Josephson junctions of multiple superconducting wires, Phys. Rev. B **97**, 174518 (2018).
[23] B. Venitucci, D. Feinberg, R. Mélin, and B. Douçot, Nonadiabatic Josephson current pumping by microwave irradiation, Phys. Rev. B **97**, 195423 (2018).
[24] L. P. Gavensky, G. Usaj, D. Feinberg, and C. A. Balseiro, Berry curvature tomography and realization of topological Haldane model in driven three-terminal Josephson junctions, Phys. Rev. B **97**, 220505(R) (2018).
[25] R. L. Klees, G. Rastelli, J. C. Cuevas, and W. Belzig, Microwave spectroscopy reveals the quantum geometric tensor of topological Josephson matter, Phys. Rev. Lett. **124**, 197002 (2020).
[26] V. Fatemi, A. R. Akhmerov, and L. Bretheau, Weyl Josepshon circuits, Phys. Rev. Res. **3**, 013288 (2021).
[27] L. Peyruchat, J. Griesmar, J.-D. Pillet, and Ç. Ö. Girit, Transconductance quantization in a topological Josephson tunnel junction circuit, Phys. Rev. Res. **3**, 013289 (2021).
[28] H. Weisbrich, R. L. Klees, G. Rastelli, and W. Belzig, Second Chern number and non-Abelian Berry phase in topological superconducting systems, PRX Quantum **2**, 010310 (2021).
[29] Y. Chen and Y. V. Nazarov, Weyl point immersed in a continuous spectrum: An example from superconducting nanostructures, Phys. Rev. B **104**, 104506 (2021).
[30] Y. Chen and Y. V. Nazarov, Spin-Weyl quantum unit: theoretical proposal, Phys. Rev. B **103**, 045410 (2021).
[31] E. V. Repin and Y. V. Nazarov, Weyl points in multiterminal hybrid superconductor-semiconductor nanowire devices, Phys. Rev. B **105**, L041405 (2022).
[32] L. Peralta Gavensky, G. Usaj, and C. A. Balseiro, Multiterminal Josephson junctions: A road to topological flux networks, Europhys. Lett. **141**, 36001 (2023).
[33] J. D. Pillet, V. Benzoni, J. Griesmar, J.-L. Smirr, and Ç. Ö. Girit, Nonlocal Josephson effect in Andreev molecules, Nano Lett. **19**, 7138 (2019).
[34] J.-D. Pillet, V. Benzoni, J. Griesmar, J.-L. Smirr, and Ç. Ö. Girit, Scattering description of Andreev molecules, SciPost Phys. Core **2**, 009 (2020).
[35] V. Kornich, H. S. Barakov, and Yu. V. Nazarov, Fine energy splitting of overlapping Andreev bound states in multiterminal superconducting nanostructures, Phys. Rev. Res. **1**, 033004 (2019).
[36] J.-D. Pillet, S. Annabi, A. Peugeot, H. Riechert, E. Arrighi, J. Griesmar, and L. Bretheau, Josephson Diode effect in Andreev molecules, Phys. Rev. Res. **5**, 033199 (2023).
[37] A. H. Pfeffer, J. E. Duvauchelle, H. Courtois, R. Mélin, D. Feinberg, and F. Lefloch, Subgap structure in the conductance of a three-terminal Josephson junction, Phys. Rev. B **90**, 075401 (2014).
[38] Y. Cohen, Y. Ronen, J. H. Kang, M. Heiblum, D. Feinberg, R. Mélin, and H. Strikman, Nonlocal supercurrent of quartets in a three-terminal Josephson junction, Proc. Natl. Acad. Sci. USA **115**, 6991 (2018).
[39] K. F. Huang, Y. Ronen, R. Mélin, D. Feinberg, K. Watanabe, T. Taniguchi, and P. Kim, Evidence for 4e charge of Cooper quartets in a biased multi-terminal graphene-based Josephson junction, Nat. Commun. **13**, 3032 (2022).
[40] G. V. Graziano, M. Gupta, M. Pendharkar, J. T. Dong, C. P. Dempsey, C. Palmstrøm, and V. S. Pribiag, Selective control of conductance modes in multi-terminal Josephson junctions, Nat. Commun. **13**, 5933 (2022).
[41] S. Park, W. Lee, S. Jang, Y.-B. Choi, J. Park, W. Jung, K. Watanabe, T. Taniguchi, G. Y. Cho, and G.-H. Lee, Steady Floquet-Andreev states in graphene Josephson junctions, Nature (London) **603**, 421 (2022).

[42] O. Kürtössy, Z. Scherübl, G. Fülöp, I. E. Lukács, T. Kanne, J. Nygard, P. Makk, and S. Csonka, Andreev molecule in parallel InAs nanowires, Nano Lett. **21**, 7929 (2021).

[43] M. Coraiola, D. Z. Haxell, D. Sabonis, H. Weisbrich, A. E. Svetogorov, M. Hinderling, S. C. ten Kate, E. Cheah, F. Krizek, R. Schott, W. Wegscheider, J. C. Cuevas, W. Belzig, and F. Nichele, Hybridisation of Andreev bound states in three-terminal Josephson junctions, Nat. Commun. **14**, 6784 (2023).

[44] S. Matsuo, T. Imoto, T. Yokoyama, Y. Sato, T. Lindemann, S. Gronin, G. C. Gardner, S. Nakosai, Y. Tanaka, M. J. Manfra, and S. Tarucha, Phase-dependent Andreev molecules and superconducting gap closing in coherently-coupled Josephson junctions, Nat. Commun. **14**, 8271 (2023).

[45] S. Matsuo, T. Imoto, T. Yokoyama, Y. Sato, T. Lindemann, S. Gronin, G. C. Gardner, M. J. Manfra, and S. Tarucha, Engineering of anomalous Josephson effect in coherently coupled Josephson junctions, Sci. Adv. **9**, eadj3698 (2023).

[46] M. Gupta, G. V. Graziano, M. Pendharkar, J. T. Dong, C. P. Dempsey, C. Palmstrøm, and V. S. Pribiag, Superconducting diode effect in a three-terminal Josephson device, Nat. Commun. **14**, 3078 (2023).

[47] F. Zhang, M. T. Ahari, A. S. Rashid, G. J. de Coster, T. Taniguchi, K. Watanabe, M. J. Gilbert, N. Samarth, and M. Kayyalha, Reconfigurable magnetic-field-free superconducting diode effect in multi-terminal Josephson junctions, arXiv:2301.05081.

[48] A. W. Draelos, M.-T. Wei, A. Seredinski, H. Li, Y. Mehta, K. Watanabe, T. Taniguchi, I. V. Borzenets, F. Amet, and G. Finkelstein, Supercurrent flow in multiterminal graphene Josephson junctions, Nano Lett. **19**, 1039 (2019).

[49] N. Pankratova, H. Lee, R. Kuzmin, K. Wickramasinghe, W. Mayer, J. Yuan, M. Vavilov, J. Shabani, and V. Manucharyan, The multi-terminal Josephson effect, Phys. Rev. X **10**, 031051 (2020).

[50] G. V. Graziano, J. S. Lee, M. Pendharkar, C. Palmstrøm, and V. S. Pribiag, Transport studies in a gate-tunable three-terminal Josephson junction, Phys. Rev. B **101**, 054510 (2020).

[51] E. G. Arnault, T. Larson, A. Seredinski, L. Zhao, H. Li, K. Watanabe, T. Taniguchi, I. Borzenets, F. Amet, and G. Finkelstein, The multiterminal inverse AC Josephson effect, Nano Lett. **21**, 9668 (2021).

[52] S. A. Khan, L. Stampfer, T. Mutas, J.-H. Kang, P. Krogstrup, and T. S. Jespersen, Multiterminal quantized conductance in InSb nanocrosses, Adv. Mater. **33**, 2100078 (2021).

[53] E. G. Arnault, S. Idris, A. McConnell, L. Zhao, T. F. Q. Larson, K. Watanabe, T. Taniguchi, G. Finkelstein, and F. Amet, Dynamical stabilization of multiplet supercurrents in multi-terminal Josephson junctions, Nano Lett. **22**, 7073 (2022).

[54] S. Matsuo, J. S. Lee, C.-Y. Chang, Y. Sato, K. Ueda, C. J. Palstrøm, and S. Tarucha, Observation of the nonlocal Josephson effect on double InAs nanowires, Commun. Phys. **5**, 221 (2022).

[55] F. Zhang, A. S. Rashid, M. T. Ahari, W. Zhang, K. M. Ananthanarayanan, R. Xiao, G. J. de Coster, M. J. Gilbert, N. Samarth, and M. Kayyalha, Andreev processes in mesoscopic multiterminal graphene Josephson junctions, Phys. Rev. B **107**, L140503 (2023).

[56] J. M. Rowell, Magnetic field dependence of the Josephson tunnel current, Phys. Rev. Lett. **11**, 200 (1963).

[57] R. C. Dynes and T. A. Fulton, Supercurrent density distribution in Josephson junctions, Phys. Rev. B **3**, 3015 (1971).

[58] H. H. Zappe, Determination of the current density distribution in Josephson tunnel junctions, Phys. Rev. B **11**, 2535 (1975).

[59] A. Barone and G. Paterno, *Physics and Applications of the Josephson Effect* (Wiley, New York, 1982).

[60] M. Tinkham, *Introduction to Superconductivity*, 2nd ed. (McGraw-Hill, New York, 1996).

[61] V. Barzykin and A. M. Zagoskin, Coherent transport and nonlocality in mesoscopic SNS junctions: Anomalous magnetic interference patterns, Superlatt. Microstruct. **25**, 797 (1999).

[62] K. Kikuchi, H. Myoren, T. Iizuka, and S. Takada, Normal-distribution function- shaped Josephson tunnel junctions, Appl. Phys. Lett. **77**, 3660 (2000).

[63] L. Angers, F. Chiodi, G. Montambaux, M. Ferrier, S. Guéron, H. Bouchiat, and J. C. Cuevas, Proximity dc squids in the long-junction limit, Phys. Rev. B **77**, 165408 (2008).

[64] F. Chiodi, M. Ferrier, S. Guéron, J. C. Cuevas, G. Montambaux, F. Fortuna, A. Kasumov, and H. Bouchiat, Geometry-related magnetic interference patterns in long *SNS* Josephson junctions, Phys. Rev. B **86**, 064510 (2012).

[65] M. Amado, A. Fornieri, F. Carillo, G. Biasiol, L. Sorba, V. Pellegrini, and F. Giazotto, Electrostatic tailoring of magnetic interference in quantum point contact ballistic Josephson junctions, Phys. Rev. B **87**, 134506 (2013).

[66] S. Hart, H. Ren, T. Wagner, P. Leubner, M. Mühlbauer, C. Brüne, H. Buhmann, L. W. Molenkamp, and A. Yacoby, Induced superconductivity in the quantum spin Hall edge, Nat. Phys. **10**, 638 (2014).

[67] M. T. Allen, O. Shtanko, I. C. Fulga, A. R. Akhmerov, K. Watanabe, T. Taniguchi, P. Jarillo-Herrero, L. S. Levitov, and A. Yacoby, Spatially resolved edge currents and guided-wave electronic states in graphene, Nat. Phys. **12**, 128 (2016).

[68] F. Amet, C. T. Ke, I. V. Borzenets, J. J. Wang, K. Watanabe, T. Taniguchi, R. S. Deacon, M. Yamamoto, Y. Bomze, S. Tarucha, and G. Finkelstein, Supercurrent in the quantum Hall regime, Science **352**, 966 (2016).

[69] H. Meier, V. I. Fal'ko, and L. Glazman, Edge effects in the magnetic interference pattern of a ballistic SNS junction, Phys. Rev. B **93**, 184506 (2016).

[70] R. Kraft, J. Mohrmann, R. Du, P. B. Selvasundaram, M. Irfan, U. Nefta Kanilmaz, F. Wu, D. Beckmann, H. von Löhneysen, R. Krupke, A. Akhmerov, I. Gornyi, and R. Danneau, Tailoring supercurrent confinement in graphene bilayer weak links, Nat. Commun. **9**, 1722 (2018).

[71] M. Irfan, and A. R. Akhmerov, Geometric focusing of supercurrent in hourglass-shaped ballistic Josephson junctions, arXiv:1810.04588.

[72] P. Pandey, D. Beckmann, and R. Danneau, Energy distribution controlled ballistic Josephson junction, Phys. Rev. B **106**, 214503 (2022).

[73] C.-G. Chu, J.-J. Chen, A.-Q. Wang, Z.-B. Tan, C.-Z. Li, C. Li, A. Brinkman, P.-Z. Xiang, N. Li, Z.-C. Pan, H.-Z. Lu, D. Yu, and Z.-M. Liao, Broad and colossal edge supercurrent in Dirac semimetal Cd_3As_2 Josephson junctions, Nat. Commun. **14**, 6162 (2023).

[74] A. Melo, V. Fatemi, and A. R. Akhmerov, Multiplet supercurrent in Josephson tunneling circuits, SciPost Phys. **12**, 017 (2022).

[75] A. Zazunov, V. S. Shumeiko, E. N. Bratus', J. Lantz, and G. Wendin, Andreev level qubit, Phys. Rev. Lett. **90**, 087003 (2003).

[76] T. Meng, S. Florens, and P. Simon, Self-consistent description of Andreev bound states in Josephson quantum dot devices, Phys. Rev. B **79**, 224521 (2009).

[77] S. B. Kaplan, C. C. Chi, D. N. Langenberg, J. J. Chang, S. Jafarey, and D. J. Scalapino, Quasiparticle and phonon lifetimes in superconductors, Phys. Rev. B **14**, 4854 (1976).

[78] R. C. Dynes, V. Narayanamurti, and J. P. Garno, Direct measurement of quasiparticle-lifetime broadening in a strong-coupled superconductor, Phys. Rev. Lett. **41**, 1509 (1978).

[79] J. P. Pekola, V. F. Maisi, S. Kafanov, N. Chekurov, A. Kemppinen, Yu. A. Pashkin, O.-P. Saira, M. Möttönen, and J. S. Tsai, Environment-assisted tunneling as an origin of the Dynes density of states, Phys. Rev. Lett. **105**, 026803 (2010).

[80] O.-P. Saira, A. Kemppinen, V. F. Maisi, and J. P. Pekola, Vanishing quasiparticle density in a hybrid Al/Cu/Al single-electron transistor, Phys. Rev. B **85**, 012504 (2012).

[81] J. C. Cuevas, A. Martín-Rodero, and A. Levy Yeyati, Hamiltonian approach to the transport properties of superconducting quantum point contacts, Phys. Rev. B **54**, 7366 (1996).

[82] I. O. Kulik, Macroscopic Quantization and the proximity effect in S-N-S junctions, Zh. Eksp. Teor. Fiz. **57**, 1745 (1969) [Sov. Phys. JETP **30**, 944 (1970)].

[83] C. Ishii, Josephson currents through junctions with normal metal barriers, Prog. Theor. Phys. **44**, 1525 (1970).

[84] P. F. Bagwell, Suppression of the Josephson current through a narrow, mesoscopic, semiconductor channel by a single impurity, Phys. Rev. B **46**, 12573 (1992).

[85] J. C. Cuevas and F. S. Bergeret, Magnetic interference patterns and vortices in diffusive SNS junctions, Phys. Rev. Lett. **99**, 217002 (2007).

[86] M. Schechter, Y. Imry, and Y. Levinson, Reflectionless tunneling in ballistic normal-metal–superconductor junctions, Phys. Rev. B **64**, 224513 (2001).

[87] T. Henning, D. B. Haviland, and P. Delsing, Coulomb blockade effects in anodised niobium nanostructures, Supercond. Sci. Technol. **10**, 727 (1997).

[88] P. Delsing, C. D. Chen, D. B. Haviland, T. Bergsten, and T. Claeson, Two-dimensional arrays of low capacitance tunnel junctions: general properties, phase transitions and Hall effect, AIP Conf. Proc. **427**, 313 (1998).

[89] K. Cedergren, R. Ackroyd, S. Kafanov, N. Vogt, A. Shnirman, and T. Duty, Insulating Josephson-junction chains as pinned Luttinger liquids, Phys. Rev. Lett. **119**, 167701 (2017).